Improved Properties of Soft Magnetic Composites with Hollow Microstructures

Xiaotao Ren[1]**, Romain Corcolle**[2] **and Yves Perriard**[1]

[1] Integrated Actuators Laboratory (LAI), École Polytechnique Fédérale de Lausanne (EPFL), Neuchâtel, Switzerland

[2] Division of Engineering and Computer Science, NYU Shanghai, Shanghai, People's Republic of China

E-mail: `xiaotao.ren@epfl.ch`

20 August 2021

Abstract. Soft Magnetic Composites (SMCs) possess promising electromagnetic characteristics and attract intense research and application interest in the engineering community. Fabrication of composites with customized architecture is feasible due to the recent advances in additive manufacturing techniques. The systematic progress of computational optimization has opened up the possibility of devising such structures. This article presents newly structured SMCs which can recently be possible by additive manufacturing. The effective permeability and eddy current losses are studied in comparison to those properties of traditionally fabricated SMCs. With this hollow inclusion arrangement, for the same iron volume fraction, the effective permeability can be greatly enhanced (more than tenfold) while the eddy current losses decrease considerably. For the same magnetic property, we save iron material, make the composite lighter, and benefit from a lower level of eddy current losses with the hollow configuration.

Keywords: bi-coated assemblage, eddy current losses, effective permeability.

Submitted to: *J. Phys. D: Appl. Phys.*

1. Introduction

Composites are useful because they potentially incorporate the properties of the component materials and their use in manufacturing applications is increasing at an accelerated rate [1]. In addition to the physical properties, the microscopic arrangement of the components would contribute significantly to the macroscopic behavior of the composite [2]. The emergence of modern manufacturing techniques, analytical homogenization and multiscale numerical algorithms has boosted their development.

Soft Magnetic Composites (SMCs) exhibit outstanding electromagnetic features from their constitutive components and benefit from their architecture. They are generally composed of magnetic inclusions such as iron granules embedded in the dielectric medium [3]. Inclusions ensure magnetization capacity while the matrix confines eddy currents in each granule, which considerably reduces the losses. Increasing academic research and engineering applications are engaged in the development of SMCs[4]. SMCs are traditionally manufactured by powder metallurgy [5, 6, 7]. Research interests mainly focus on composite modelings [8, 9, 10, 11, 12, 13, 14, 15] for the effective permeability and eddy current losses. Efforts are continued on the delicate treatment in powder coating or searching new powder alloy or insulation layer so as to enhance the properties [16, 17]. Optimizing the manufacturing process and exploring new powder and matrix materials are drawing research attention [18, 19, 20]. Nevertheless, the indispensable insulation layer significantly hinders the magnetic permeability. Even for a thin insulation film and a large volume fraction of the magnetic powder of a relatively high property, the effective permeability of the composite is still quite limited. It is necessary to explore the novel composite structures with the help of additive manufacturing (AM) technology.

The rapid development of AM will boost SMC advancement by providing the capability to easily fabricate new composites [21, 22, 23]. It allows us to break through the barrier of the traditional metallurgy. Metallic 3D printing is developing fast and is becoming increasingly popular [24, 25, 26]. In this article, we study a novel SMC structure with 3D-printable hollow inclusions. The effective permeability and electrical resistance are modeled and compared with the results of SMCs with solid inclusions.

2. Novel SMC microstructure

SMCs are a lattice of inclusions immersed in an insulating medium. Since the size of the inclusion is smaller than that of the device made of SMCs, the composite is usually considered spatially periodic. For this bi-phased composite, the medium is numbered phase 1 and the inclusion phase 2. Isotropic transverse 2D and isotropic 3D composites are considered in this study which lead to three different configurations listed in table 1.

Table 1: Three configurations for the composites.

Name	Case
I	2D composite with out-of-plane field
II	2D composite with in-plane field
III	3D composite

2.1. Solid inclusion

A cell, denoted $\Omega^\alpha \subset \mathbb{R}^d (d = 2, 3)$, as shown in figure 1a, consisting of an inclusion and its portion of the matrix, is studied to understand the characteristics of the composite. The inclusion is usually simplified as a sphere, or more generally, an ellipsoid (a disk or an ellipse in 2D). To attain high concentration, the inclusion is usually considered as

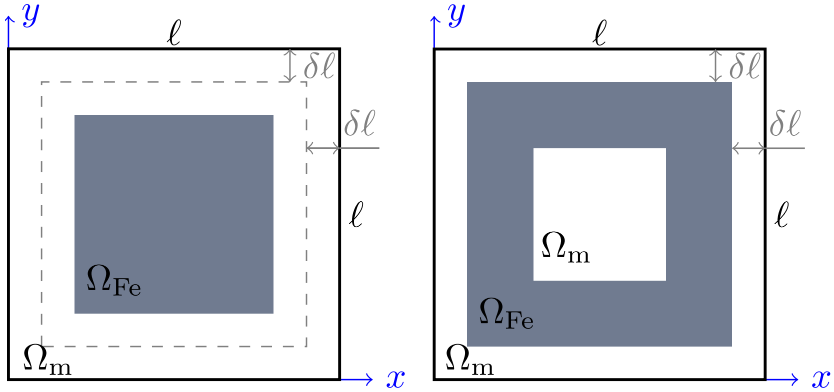

(a) Ω^{α} (b) Ω^{β}

Figure 1: Sketch of a composite cell of size ℓ with a minimal insulation film thickness $\delta\ell$. (a) SMC cell, Ω^{α}, by traditional powder metallurgy; (b) Newly structured SMC cell, Ω^{β}

a cube (a square in 2D). In this work, we consider only the cube (square) inclusion to discuss a full range of the iron material. Let χ_2 denote the volume fraction of the iron inclusion. For a small magnitude of loadings, the magnetic behavior of the constituents can be modeled with a linear constitutive law (permeability μ_1 for the matrix which is typically of non-magnetic material so its permeability value is equal to the vacuum permeability μ_0, and μ_2 for the iron).

For 2D composites (assuming infinitely long structure in the third direction), the out-of-plane effective permeability $\tilde{\mu}^{\alpha}_{\mathrm{I}}$ can be described by the Wiener upper bound:

$$\tilde{\mu}^{\alpha}_{\mathrm{I}} = \chi_2\mu_2 + (1-\chi_2)\mu_1 \tag{1}$$

The in-plane effective permeability $\tilde{\mu}^{\alpha}_{\mathrm{II}}$ in the 2D case (assuming transverse isotropy) and the isotropic effective permeability $\tilde{\mu}^{\alpha}_{\mathrm{III}}$ in the 3D case (assuming isotropy) can be accurately estimated with a classical Maxwell Garnett (MG) model [27],

$$\text{for } k = \mathrm{II}, \mathrm{III} \quad \tilde{\mu}^{\alpha}_{k} = \mu_1 + \frac{\chi_2\mu_1\left(\mu_2-\mu_1\right)}{\mu_1 + N_k\left(1-\chi_2\right)\left(\mu_2-\mu_1\right)} \tag{2}$$

with N_k the depolarization coefficients ($N_{\mathrm{II}} = 1/2$ and $N_{\mathrm{III}} = 1/3$). This estimate, originally determined for dilute ellipsoidal inclusions, also provides an accurate estimate for high volume fraction ($\chi_2 > 95\%$) of inclusions [28].

The MG estimate is a strictly increasing function with respect to the inclusion material property μ_2. If the permeability contrast is sufficiently great, the estimate actually converges toward a limit value,

$$\text{for } k = \mathrm{II}, \mathrm{III} \quad \lim_{\mu_2\to\infty} \tilde{\mu}^{\alpha}_{k} = \mu_1 + \frac{\chi_2\mu_1}{N_k(1-\chi_2)} \tag{3}$$

which does not depend of μ_2.

When the iron volume fraction reaches a maximum (while still keeping a thin insulation layer), its value is,

$$\lim_{\substack{\mu_2\to\infty\\ \delta\to 0}} \tilde{\mu}^{\alpha}_{\mathrm{II}} = \lim_{\substack{\mu_2\to\infty\\ \delta\to 0}} \tilde{\mu}^{\alpha}_{\mathrm{III}} = \frac{\mu_1}{2\delta} \tag{4}$$

which is independent of the dimension.

The option of enhancing the effective permeability of the composite by increasing the permeability of the inclusion is not applicable, especially when $\mu_2 \geq 1000\mu_1$. Another option is to increase the volume fraction of the inclusion. However, the inclusion should be well insulated to reduce the eddy current losses, which limits the increment of the inclusion volume fraction. Therefore, we propose a novel composite topology with a hollow inclusion.

2.2. Hollow inclusion

The Maxwell Garnett model (2), which accurately describes the effective permeability for composites with α microstructures, is actually equal to the lower Hashin-Shtrikman (HS) bound [29, 30]. It means that this structure provides the lowest effective permeability one can expect when exhibiting isotropy.

If the two constituents are exchanged, then the effective permeability of the composite would be the highest one (higher HS bound) when exhibiting isotropy. The expressions of HS bounds are (N is equal to 1/2 in 2D and 1/3 in 3D),

$$\begin{cases} \tilde{\mu}_{\mathrm{HS}-} &= \mu_1 + \dfrac{\chi_2}{\dfrac{1}{\mu_2-\mu_1} + \dfrac{N\,(1-\chi_2)}{\mu_1}} \\[2ex] \tilde{\mu}_{\mathrm{HS}+} &= \mu_2 + \dfrac{1-\chi_2}{\dfrac{1}{\mu_1-\mu_2} + \dfrac{N\chi_2}{\mu_2}} \end{cases} \tag{5}$$

Exchanging the constituents may increase the effective permeability but a major problem would arise; the iron phase would then percolate and since it is electrically conductive, it would generate important eddy current losses which contradicts the purpose of SMCs. However, other structures of composites may exhibit an effective permeability higher than the lower HS bound while still preventing the iron phase to percolate.

It inspires the idea for the new composite microstructure shown in figure 1b. Such a structure can exhibit a higher effective permeability than the one for the α configuration while maintaining the insulation of the iron phase (fixed size: $\delta\ell$). Denote Ω^{β} the domain of this SMC cell. The new configuration Ω^{β} is topologically different from Ω^{α}.

For 2D composites with an out-of-plane loading, the effective permeability $\tilde{\mu}^{\beta}_{\mathrm{I}}$ is still given by the Wiener upper bound

$$\tilde{\mu}^{\beta}_{\mathrm{I}} = \tilde{\mu}^{\alpha}_{\mathrm{I}} \tag{6}$$

because this component in the 2D case does not depend on the microstructure but only on the volume fraction of the iron.

The other cases of hollow inclusion with an insulation film are quite similar on several aspects to the cases of bi-coated assemblage [2, Sec. 7.4, pp.117-118] of cylinders or spheres. The effective permeability of such assemblages actually provide good estimates for the composites with the β configuration,

$$\text{for } k = \mathrm{II}, \mathrm{III} \qquad \tilde{\mu}_k^\beta = \mu_1 + \cfrac{1-\chi_1}{\cfrac{N_k\chi_1}{\mu_1} + \cfrac{1}{\mu_2 - \mu_1 + \cfrac{1-\chi_1-\chi_2}{\cfrac{N_k\chi_2}{\mu_2} - \cfrac{1-\chi_1}{\mu_2-\mu_1}}}} \tag{7}$$

with χ_1 the volume fraction of the insulation layer ($\chi_1 = 1 - (1-2\delta)^d$). It is worth mentioning that this formula encompasses the α configuration which is a specific β configuration with no core (corresponding to $\chi_1 + \chi_2 = 1$). One can notice that $\tilde{\mu}_{\mathrm{II}}^\beta$ and $\tilde{\mu}_{\mathrm{III}}^\beta$ are monotonically decreasing functions of χ_1 (in other words, strictly decreasing functions of δ). When $\delta = 0$, $\tilde{\mu}_{\mathrm{II}}^\beta$ and $\tilde{\mu}_{\mathrm{III}}^\beta$ attain the HS upper bound $\tilde{\mu}_{\mathrm{HS+}}$. The effective permeability as a function of the iron volume fraction χ_2 and the relative insulation size δ is illustrated in figure 2. A thinner outer insulation could definitely increase the effective property but it is equally critical to maintain the insulation film to confine the eddy currents for magneto-dynamics applications.

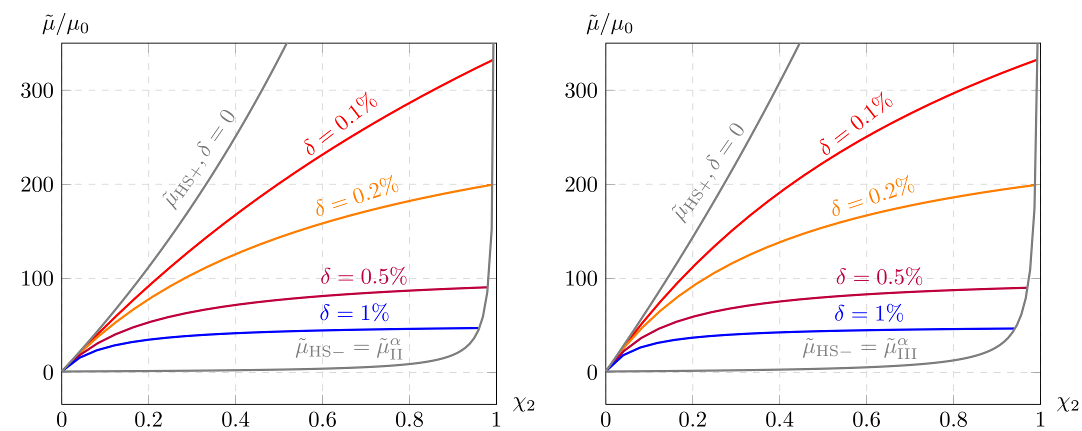

(a) 2D (case II): $\tilde{\mu}_{\mathrm{II}}^\beta$ (b) 3D (case III): $\tilde{\mu}_{\mathrm{III}}^\beta$

Figure 2: Effective permeability predicted by (7) as a function of iron volume fraction for different δ values. $\mu_2 = 1000\mu_0$ and $\mu_1 = \mu_0$.

The maximum value attained by $\tilde{\mu}_{\mathrm{II}}^\beta$ and $\tilde{\mu}_{\mathrm{III}}^\beta$ is also given by (4) when considering the large permeability contrast and a thin insulation layer.

2.3. Validation with finite element models

The bi-coated homogenization model (7) is verified by numerical calculations. It is not necessary to discuss the case I for both the α and β configurations since the Wiener upper bound is an exact solution for the effective permeability. In this section, we compare the effective permeability values predicted from (7) with those obtained by the Finite Element Method (FEM) for 2D with an in-plane magnetic field (case II) and for 3D (case III). A constant magnetic permeability $\mu_2 = 1000\mu_0$ is used for the iron and magneto-static calculations are carried out to determine the effective permeability of the composite. In the following, the effective permeability $\tilde{\mu}_{\mathrm{FEM}}$ determined by FEM will be considered as the reference result.

For the α case, the inclusion is a square in order to span the largest possible range of volume fractions for the iron. Similarly, for the β case, the hollow geometry inside the iron material is also a square. The comparison between the analytical estimates and the FEM values of the effective permeability is presented in figure 3.

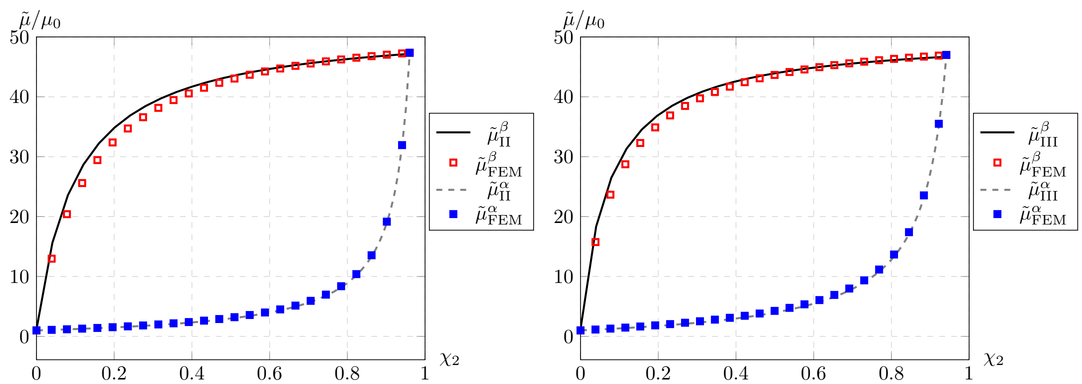

(a) 2D case $\tilde{\mu}^{\alpha}_{\mathrm{II}}$ and $\tilde{\mu}^{\beta}_{\mathrm{II}}$

(b) 3D case $\tilde{\mu}^{\alpha}_{\mathrm{III}}$ and $\tilde{\mu}^{\beta}_{\mathrm{III}}$

Figure 3: Comparison of the effective permeability predicted by (7) with the one determined by FEM as a function of the volume fraction of iron. $\mu_2 = 1000\mu_0$, $\mu_1 = \mu_0$, and $\delta = 1\%$.

It can be observed that, for the same volume fraction of the iron, the β arrangement exhibits a much better magnetic property than the α one. The effective permeability of the α arrangement varies closely along the HS lower bound. At high volume fraction ($\chi_2 \sim 0.90$), the effective permeability for the α arrangement can drop sharply for a small volume fraction decrease (when trying to use less iron material) while the β configuration can maintain the same level of permeability value.

To evaluate the accuracy of the analytical models, the relative error is defined by

$$\eta_\mu = \frac{\tilde{\mu} - \tilde{\mu}_{\mathrm{FEM}}}{\tilde{\mu}_{\mathrm{FEM}}} \times 100\%. \tag{8}$$

The errors are plotted in figure 4. It shows that the MG model (2) underestimates the effective permeability for all the volume fraction range in the α configuration. On the other hand, for the β configuration, the errors decrease with the volume fraction. The bi-coated model (7) generally overestimates the effective permeability for low volume fractions. It is interesting to observe that for a major part of the range of volume fractions, ($\chi_2 > 0.35$ for $\delta = 1\%$, and $\chi_2 > 0.50$ for $\delta = 0.5\%$), the relative error is below 3% which means the bi-coated analytical model is accurate for estimating the effective permeability for β microstructures.

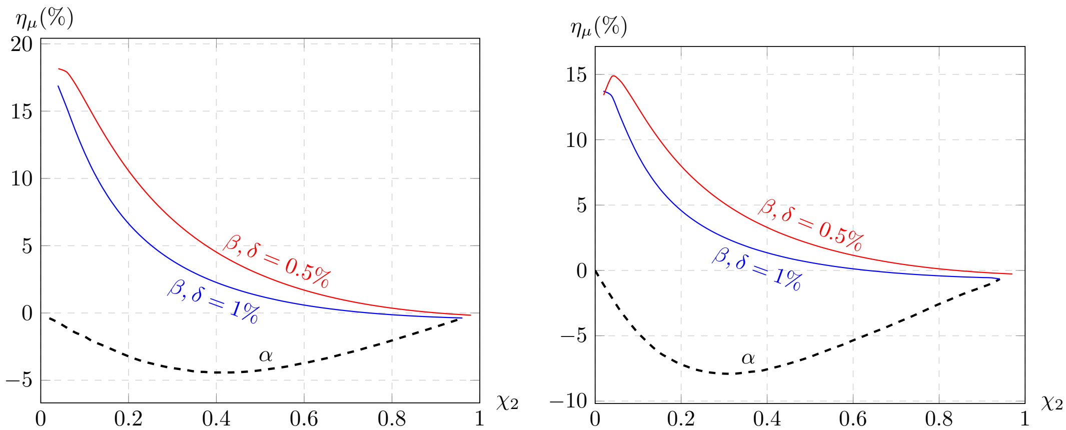

(a) 2D (case II) (b) 3D (case III)

Figure 4: Relative errors (8) as a function of the volume fraction of the iron. $\mu_2 = 1000\mu_0$ and $\mu_1 = \mu_0$.

It is worth noticing that at low iron filling factor, the analytical model for the β configuration is less accurate. But since high effective magnetic permeability is expected, attention is mainly focused on high volume fraction of the iron where the bi-coated model (7) predicts accurately.

3. Eddy current losses

Eddy current circulates in electrically conductive parts when loaded with an alternating magnetic field. According to Faraday's law, an alternating magnetic field generates an electromotive force (emf), which produces an electric field $\mathbf{E}$. In a geometric domain Ω with electric conductivity σ, eddy current arises, which causes Joule heat known as the eddy current losses. The definition of the volumetric loss density Q is the Joule losses dissipated per unit volume,

$$Q = \frac{1}{2|\Omega|} \int_\Omega \sigma \mathbf{E}^2 \mathrm{d}\Omega \tag{9}$$

where $|\Omega|$ indicates the volume of the domain Ω. At low working frequency, the losses are proportional to the conductivity, the square of the induction magnitude (B_0), the square of the frequency (f), and the square of the dimension [8, 31]. Define

$$Q_0 = \pi^2 \sigma f^2 \ell^2 B_0^2 \tag{10}$$

so that $Q = KQ_0$, where K is a shape and volume fraction dependent dimensionless factor.

3.1. Solid inclusion

Eddy current losses for composites with solid inclusions of different shapes have already been examined in various studies (see for instance [8, 9, 13, 32]). The analytical formulae derived in these studies are based on the assumption of uniform magnetic induction in the iron particles, which is verified for high volume fractions. For square or cubic inclusions, the homogenized eddy current losses of the composites are estimated with:

$$\begin{cases} Q_{\mathrm{I}}^{\alpha} = \dfrac{9}{128}\left(\dfrac{\chi_2\,\mu_2}{\chi_2\,\mu_2+(1-\chi_2)\mu_1}\right)^2 Q_0 \\ Q_{\mathrm{II}}^{\alpha} = \dfrac{2}{3}\left(\dfrac{\chi_2\,\mu_2}{(1+\chi_2)\mu_2+(1-\chi_2)\mu_1}\right)^2 Q_0 \\ Q_{\mathrm{III}}^{\alpha} = \dfrac{81}{128}\dfrac{1}{\sqrt[3]{\chi_2}}\left(\dfrac{\chi_2\,\mu_2}{(1+2\chi_2)\mu_2+2(1-\chi_2)\mu_1}\right)^2 Q_0 \end{cases} \tag{11}$$

Simpler expressions can also be derived when considering large contrasts:

$$\begin{cases} Q_{\mathrm{I}}^{\alpha} \approx \dfrac{9}{128}Q_0 \\ Q_{\mathrm{II}}^{\alpha} \approx \dfrac{2}{3}\left(\dfrac{\chi_2}{1+\chi_2}\right)^2 Q_0 \\ Q_{\mathrm{III}}^{\alpha} \approx \dfrac{81}{128}\dfrac{\chi_2^{5/3}}{(1+2\chi_2)^2}Q_0 \end{cases} \tag{12}$$

3.2. Hollow inclusions

For hollow inclusions, the eddy current loss models are more complex to determine because the magnetic induction in the iron inclusion is not uniform (except for the case I). Similarly to the strategy used for effective permeability in Section 2, we will use an equivalent bi-coated cylinder/sphere to determine analytical formulae for the eddy current losses of composites with the β microstructure.

The analytical formulae are (see Appendix for a detailed derivation):

$$\begin{cases} Q_{\mathrm{I}}^{\beta} = \dfrac{9}{128}\Phi Q_0 \\ Q_{\mathrm{II}}^{\beta} = \dfrac{2}{3}\left(\dfrac{1-\chi_1}{2-\chi_1}\right)^2 \Phi Q_0 \\ Q_{\mathrm{III}}^{\beta} = \dfrac{81}{128}\dfrac{(1-\chi_1)^{5/3}}{(3-2\chi_1)^2}\Phi_{\mathrm{III}} Q_0 \end{cases} \tag{13}$$

with Φ and Φ_{III} the dimensionless coefficients depending on the volume fractions and the permeability contrast (see Appendix for the exact expressions).

The eddy current losses calculated from (13) are illustrated in figure 5 for different δ values. It can be observed that as the insulation becomes thinner (δ decreases), eddy current losses slightly decrease for I, II, III cases. As opposed to the effective permeability which is quite sensitive to δ values, the effect of δ on the eddy current losses is negligible for these three cases (maximum relative difference is 7%, 3%, and 10% respectively for these three cases for the considered δ values in this study).

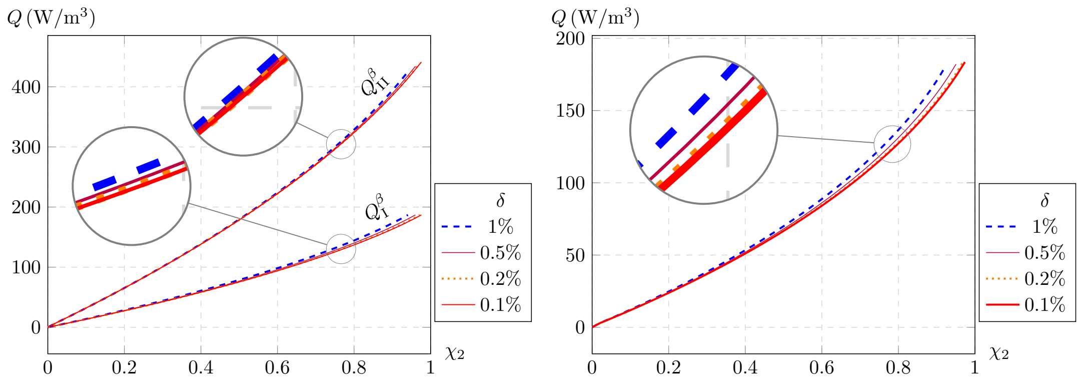

(a) 2D cases Q_{I}^{β} and Q_{II}^{β} (b) 3D case Q_{III}^{β}

Figure 5: The theoretical eddy current losses as a function of iron volume fraction for different δ values. $\sigma_{\mathrm{Fe}} = 1.12 \times 10^7$ S/m, $\mu_2 = 1000\mu_0$, $\mu_1 = \mu_0$, and $f = 100$ Hz.

3.3. Validation with finite element models

Harmonic computations of unit cells of composites in the α and β configurations have been performed by FEM and eddy current losses can be post-processed from these computations. Similarly to the effective permeability, the influence of volume fraction of the iron χ_2 is particularly studied. In order to evaluate the accuracy of the analytical estimates, an error indicator is also verified. The relative error is defined by

$$\eta_Q = \frac{Q - Q_{\mathrm{FEM}}}{Q_{\mathrm{FEM}}} \times 100\% \tag{14}$$

In the FEM and analytical calculations, the parameters as detailed in table 2 have been used. The eddy current losses for the α and β microstructures in the I, II, and III cases are illustrated in figure 6.

Table 2: List of parameters used for the validation with FEM.

Parameter (unit)	Value
B_0 (T)	1
f (Hz)	100
σ_{Fe} (S/m)	1.12×10^7
ℓ (μm)	50
δ (%)	1
μ_1/μ_0 (-)	1
μ_2/μ_0 (-)	1000

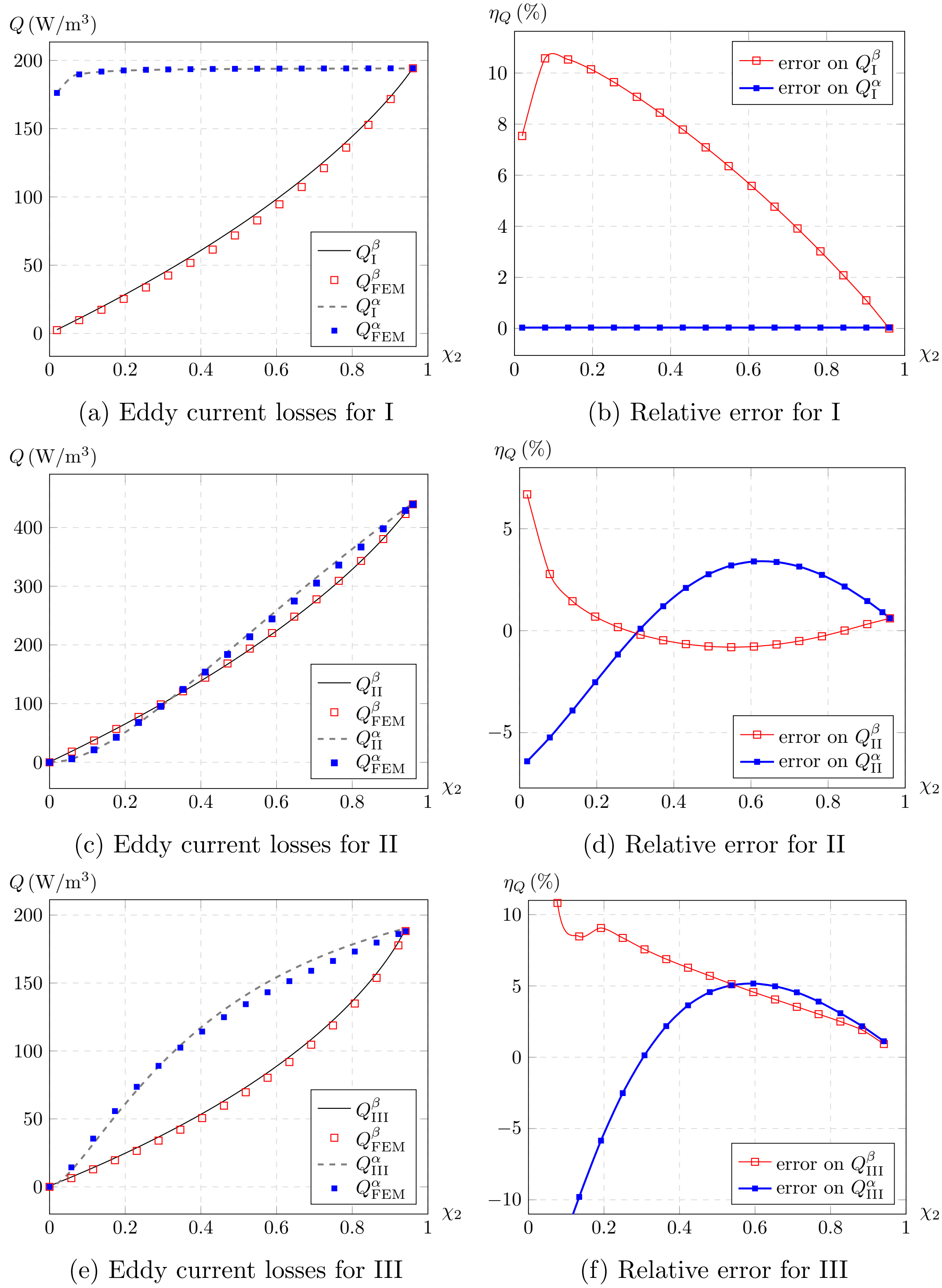

(a) Eddy current losses for I
(b) Relative error for I
(c) Eddy current losses for II
(d) Relative error for II
(e) Eddy current losses for III
(f) Relative error for III

Figure 6: Eddy current losses as a function of the volume fraction of iron in the I, II, and III cases.

It can be seen that the α configuration exhibits a constant (except at very low filling factors) eddy current loss density, while the losses in the β case are a quasi-linear function of the iron volume fraction for the case I. Another conclusion which can be drawn is the fact that the losses are generally lower in the β configuration than in the α one for a given volume fraction of the iron (which means with the same effective permeability in the case I).

It also appears that the analytical models provide an accurate estimate of the losses for both the α and β configurations in case I. The formula Q_{I}^{α} estimates perfectly the eddy current losses in α configuration with a relative error always below 0.035%. The Q_{I}^{β} estimate is accurate at high volume fractions but is less accurate (still generally less than 10%) for low volume fractions. This is due to the fact that the equivalent bi-coated cylinder used to derive the formula does not fully capture the path of eddy currents in a hollow square, hence the slight error in the analytical estimate.

For the case II, it can be observed that the β composites dissipate roughly the same amount of energy as the α ones. At high volume fraction ($\chi_2 > 0.3$), the β composites have a slightly better loss characteristic than the α ones. At low volume fraction, the opposite phenomenon is observed. For both the α and β composites the eddy current losses are roughly a quasi-linear function of the iron volume fraction.

Once again, the analytical formulae are quite accurate in the case II since the error stays below 5% for the majority of the iron volume fraction ($\chi_2 > 10\%$). It can also be noticed that the analytical formula for the losses in the β configuration is accurate to 1% (except for very low volume fractions).

For the case III, we observe that for the whole iron volume fraction range, the β composites dissipate less energy than the α ones. When we decrease slightly the iron material at high volume fraction, the eddy current losses would decrease more for the β composites than for the α ones which is exactly the opposite to what is observed for the effective permeability. It means that the β configuration can maintain a higher permeability than the α one while exhibiting much lower losses. For the majority of the volume fraction range ($\chi_2 > 0.3$), the analytical estimates predict accurately the losses, with an error below 8%.

4. Comparison

One potential interest for SMC designers could be to use less iron in the composite in order to reduce the material cost and also to reduce the material density. Removing iron means increasing the insulation layer for the α configuration, while it means increasing the epoxy core in the center (but maintaining the insulation layer) for the β one.

All the previous results are plotted as a function of the iron volume fraction. But it could be useful to compare the α and β configurations for the same effective permeability.

The iron saving ratio η_2 defined as,

$$\eta_2 = \frac{\chi_2^{\alpha} - \chi_2^{\beta}}{\chi_2^{\alpha}} \tag{15}$$

is plotted in figure 7 for the case II and case III problems. There is no need to calculate η_2 for the case I because both the α and β composites in the case I exhibit the same permeability for the same volume fraction.

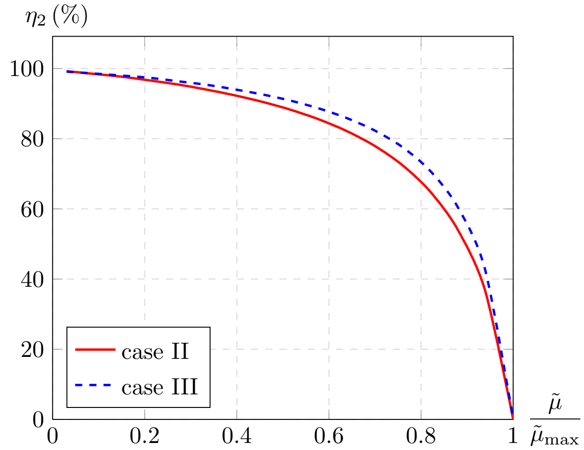

Figure 7: Iron material saving ratio as a function of effective permeability for $\delta = 1\%$.

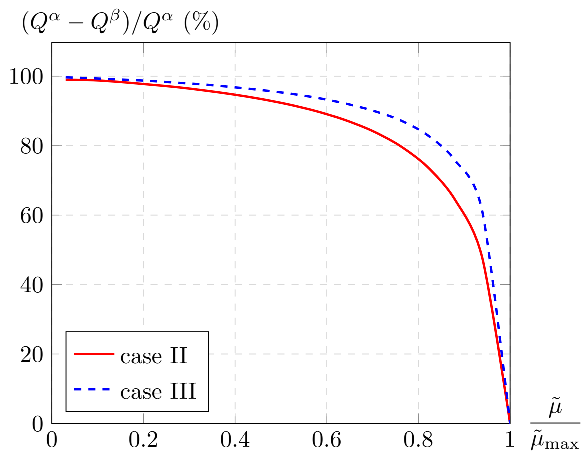

Figure 8: The quantitative loss decrease as a function of normalized effective permeability for $\delta = 1\%$.

It can be observed that as the effective permeability decreases, the material saving increases. As an example, with the goal of attaining 90% of the maximal effective permeability, this figure shows that the β composites require $50 \sim 60\%$ less iron than α composites when $\delta = 1\%$. Even more iron saving could be obtained with smaller values of δ but then macroscopic eddy currents would flow between the different cells and should not be neglected anymore.

Likewise, the quantitative loss decrease as a function of normalized effective permeability is drawn in figure 8.

Similarly to the conclusion about iron saving, it shows that β composites exhibit a much lower loss level than α composites for a given effective permeability. With the same example of 90% of the maximum effective permeability, the β composites exhibit $55 \sim 75\%$ less losses than the α composites.

It can be observed in figure 9 that the β configuration dissipates significantly less energy for the same effective permeability. At high effective values, a slight compromise

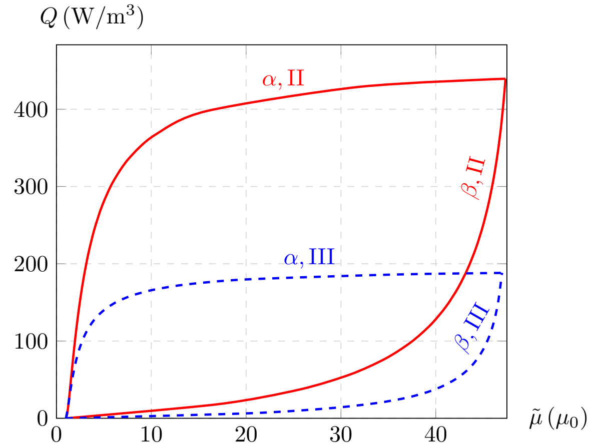

Figure 9: Eddy current losses mapping to the effective permeability for $\delta = 1\%$.

of permeability can lead to a sharp reduction in the eddy current losses for the β configuration. In comparison, also at high permeability range, the eddy current losses for the α configuration remain virtually flat for a small variation of effective permeability.

5. Conclusion

We present a new topology of soft magnetic composites with hollow microstructures. The effective permeability and eddy current losses are studied and modelled for the new structure. The models are verified by numerical results. The permeability and losses of the new structure are compared with those of the traditional one. The new structure has a stable effective permeability at high volume fractions of the iron when the fraction slightly varies. Meanwhile, for the whole fraction range, the new structure dissipates less energy. A third advantage is that the new structure can significantly save iron material for the same permeability requirement.

Appendix: Formulae for eddy current losses

Appendix A.1. Low frequency assumption

In order to predict the EC loss density of the composite, the induced electric field distribution in the iron phase (the only electrically conductive constituent in the composite) needs to be determined (see (9)). The induced electric field $\mathbf{E}$ can be related to the vector potential $\mathbf{A}$ (with $\mathbf{B} = \nabla \times \mathbf{A}$):

$$\mathbf{E} = -j\omega\mathbf{A} \tag{A.1}$$

Assuming the frequency is low enough, the induced current density does not strongly influence the magnetic induction and field distribution. It means that a quasi-static situation accurately represents the magnetic induction distribution for the dynamic case as long as the skin effect does not appear. That is the reason why the

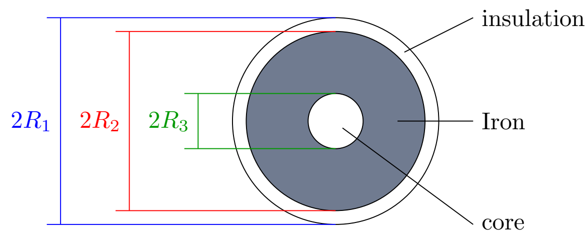

Figure A1: Equivalent doubly coated cylinder/sphere assemblage.

induced EC losses will be derived from a potential vector $\mathbf{A}$ determined in a quasi-static situation.

$$Q = \frac{\omega^2}{2|\Omega|} \int_{\Omega} \sigma \mathbf{A}^2 \mathrm{d}\Omega \tag{A.2}$$

Since only the iron phase exhibits electrical conductivity (σ), it is equal to:

$$Q = \frac{2\sigma\pi^2 f^2}{|\Omega|} \int_{\Omega_{\mathrm{Fe}}} \mathbf{A}^2 \mathrm{d}\Omega \tag{A.3}$$

For solid inclusions (α configuration), one can easily construct some EC loss density estimates (see (11) and (12)) which show a very good accuracy as long as the assumption of uniform magnetic induction in the iron phase is verified. For hollow inclusions (β configuration), such estimates are more complex to build because the magnetic induction in the iron phase varies locally and highly depends on the microstructure, which means the potential vector $\mathbf{A}$ is usually more difficult to determine.

Appendix A.2. Equivalent bi-coated cylinder/sphere composite

Hollow inclusions microstructures (β configuration) are difficult to handle analytically. Instead, an equivalent doubly coated cylinder (in 2D) or sphere (in 3D) assemblage, as shown in figure A1, will be used for determining the EC losses. Such an equivalent problem was already used to determine the effective permeability for β composites (see (7)).

The ratios of the radii R_1, R_2 and R_3 are fixed so that the volume fractions for each phase correspond to the ones in the real hollow composite problem.

$$\left(\frac{R_2}{R_1}\right)^d = 1 - \chi_1, \left(\frac{R_3}{R_1}\right)^d = 1 - \chi_1 - \chi_2 \tag{A.4}$$

with d the dimension of the problem.
Another identity can be given by introducing a relative volume fraction p (with $p = \chi_2 / (1 - \chi_1)$):

$$\left(\frac{R_3}{R_2}\right)^d = 1 - p \tag{A.5}$$

Appendix A.3. 2D hollow problem: out-of-plane magnetic field

The out-of-plane magnetic field being uniform in the whole assemblage, the corresponding magnetic induction in each phase can be easily retrieved:

$$\begin{cases} B_{1,z} = B_{3,z} = \dfrac{1}{1-\chi_2+\chi_2 c} B_0 = \gamma_{\mathrm{I}} B_0 \\ B_{2,z} = \dfrac{c}{1-\chi_2+\chi_2 c} B_0 = c\gamma_{\mathrm{I}} B_0 \end{cases} \tag{A.6}$$

with c the contrast of permeabilities ($c = \mu_2/\mu_1$) and B_0 the magnitude of the macroscopic induction.

Due to the revolution symmetry of such a problem, the vector potential $\mathbf{A}$ only exhibits an azimuthal component A_θ which only depends on r in cylindrical coordinate system (r,θ,z). Its general form is:

$$A_\theta(r) = \left(a'r - \frac{b'}{r}\right) \tag{A.7}$$

and

$$B_z = \frac{1}{r}\frac{\partial r A_\theta(r)}{\partial r} = 2a' \rightarrow a' = \frac{B_z}{2} \tag{A.8}$$

The two coefficients a' and b' are different for each phase of the composite. It should also be noted that b' is null in the core.

In the iron phase, A_θ will be written as:

$$A_\theta(r) = \frac{c\gamma_{\mathrm{I}} B_0}{2}\left(ar - \frac{bR_3^2}{r}\right) \tag{A.9}$$

a and b are dimensionless coefficients which can be determined by knowing the induction $B_{2,z}$ in the phase and also ensuring the continuity of the potential vector at the interface with the core ($r = R_3$). It gives:

$$\begin{cases} a = 1 \\ \dfrac{c\gamma_{\mathrm{I}} B_0}{2}(a-b)R_3 = \dfrac{\gamma_{\mathrm{I}} B_0}{2} R_3 \rightarrow b = 1 - \dfrac{1}{c} \end{cases} \tag{A.10}$$

The volumetric loss density $Q_{\mathrm{I}}^{\mathrm{bi}}$ can be obtained by using (A.3):

$$Q_{\mathrm{I}}^{\mathrm{bi}} = \frac{2\sigma\pi f^2}{R_1^2}\int_{R_3}^{R_2}\int_0^{2\pi} A_\theta(r)^2 r dr d\theta \tag{A.11}$$

which expands to:

$$Q_{\mathrm{I}}^{\mathrm{bi}} = \frac{c^2\gamma_{\mathrm{I}}^2}{R_1^2}\sigma\pi^2 f^2 B_0^2 \int_{R_3}^{R_2}\left(ar - \frac{bR_3^2}{r}\right)^2 r dr \tag{A.12}$$

Using the identities of the radii ratios, the EC loss density is:

$$Q_{\mathrm{I}}^{\mathrm{bi}} = \frac{1}{4}(1-\chi_1)^2 c^2\gamma_{\mathrm{I}}^2 \lambda R_1^2 \sigma\pi^2 f^2 B_0^2 \tag{A.13}$$

with λ a dimensionless parameter equal to:

$$\lambda = a^2 - (1-p)^2\left(a^2 + \frac{4abp}{1-p} + 2b^2\ln(1-p)\right) \tag{A.14}$$

Appendix A.4. 2D hollow problem: in-plane magnetic field

Assuming that the macroscopic magnetic induction $\overline{\mathbf{B}}$ is along the $\mathbf{x}$ direction (magnitude B_0), the uniform magnetic induction in the core $B_{3,x}$ is:

$$B_{3,x} = \frac{1}{1 + \frac{p}{4}(c-1)\left(2 - \chi_1\left(1 + \frac{1}{c}\right)\right)} B_0 = \gamma_{\mathrm{II}} B_0 \tag{A.15}$$

In this case, the vector potential $\mathbf{A}$ in the assemblage only exhibits an out-of-plane component A_z which can be analytically expressed in a simple form in cylindrical coordinates:

$$A_z(r,\theta) = \left(a'r - \frac{b'}{r}\right)\sin\theta \tag{A.16}$$

and

$$\begin{cases} B_r = \dfrac{1}{r}\dfrac{\partial A_z(r,\theta)}{\partial\theta} = \left(a' - \dfrac{b'}{r^2}\right)\cos\theta \\ B_\theta = -\dfrac{\partial A_z(r,\theta)}{\partial r} = \left(a' + \dfrac{b'}{r^2}\right)\sin\theta \end{cases} \tag{A.17}$$

with again a' and b' two coefficients which are different in each phase. (b' is null in the core)

In the iron phase, A_z will be written as:

$$A_z(r,\theta) = \frac{c\gamma_{\mathrm{II}}B_0}{2}\left(ar - \frac{bR_3^2}{r}\right)\sin\theta \tag{A.18}$$

a and b can be determined by considering the continuity of the normal induction and the continuity of the tangential magnetic field at the interface with the core (which exhibits a uniform field $B_{3,x} = \gamma_{\mathrm{II}}B_0$):

$$\begin{cases} \dfrac{c\gamma_{\mathrm{II}}B_0}{2}(a-b) = \gamma_{\mathrm{II}}B_0 \quad \rightarrow \quad a - b = \dfrac{2}{c} \\ \dfrac{c\gamma_{\mathrm{II}}B_0}{2}(a+b) = c\gamma_{\mathrm{II}}B_0 \quad \rightarrow \quad a + b = 2 \end{cases} \tag{A.19}$$

which gives:

$$\begin{cases} a = 1 + \dfrac{1}{c} \\ b = 1 - \dfrac{1}{c} \end{cases} \tag{A.20}$$

It should be noted that these coefficients are very similar to the ones determined in the previous section (b is identical and a is slightly different but is actually the same when considering large contrast of permeabilities which is the case here).

Since A_z is a very similar function compared to A_θ in the previous section, the EC loss density $Q_{\mathrm{II}}^{\mathrm{bi}}$ is also very similar to $Q_{\mathrm{I}}^{\mathrm{bi}}$:

$$Q_{\mathrm{II}}^{\mathrm{bi}} = \frac{1}{8}(1-\chi_1)^2 c^2\gamma_{\mathrm{II}}^2\lambda R_1^2\sigma\pi^2 f^2 B_0^2 \tag{A.21}$$

with the same formula for the dimensionless parameter λ (with the same b coefficient but a is slightly different).
It should also be noted that the coefficient in the denominator is different because of the integral of $\sin^2\theta$ in this case.

Appendix A.5. 3D hollow problem

Assuming that the macroscopic magnetic induction $\overline{\mathbf{B}}$ is along the $\mathbf{z}$ direction (magnitude B_0), the uniform magnetic induction in the core B_3 is:

$$B_3 = \frac{1}{1 + \frac{2p}{9}(c-1)\left(3 - \chi_1\left(2 + \frac{1}{c}\right)\right)} B_0 = \gamma_{\mathrm{III}} B_0 \tag{A.22}$$

In this case, the vector potential $\mathbf{A}$ in the assemblage only exhibits an azimuthal component A_θ which can be analytically expressed in a simple form in spherical coordinates (r, θ, ϕ):

$$A_\phi(r,\theta) = \left(a'r - \frac{b'}{r^2}\right)\sin\theta \tag{A.23}$$

and

$$\begin{cases} B_r = \dfrac{1}{r\sin\theta}\dfrac{\partial A_\phi(r,\theta)\sin\theta}{\partial\theta} = 2\left(a' - \dfrac{b'}{r^3}\right)\cos\theta \\ B_\theta = -\dfrac{1}{r}\dfrac{\partial r A_\phi(r,\theta)}{\partial r} = -2\left(a' + \dfrac{b'}{2r^3}\right)\sin\theta \end{cases} \tag{A.24}$$

with again a' and b' two coefficients which are different in each phase. (b' is null in the core)
In the iron phase, A_ϕ will be written as:

$$A_\phi(r,\theta) = \frac{c\gamma_{\mathrm{III}}B_0}{3}\left(ar - \frac{bR_3^3}{r^2}\right)\sin\theta \tag{A.25}$$

a and b can be determined by considering the continuity of the normal induction (at $\theta = 0$) and the continuity of the tangential magnetic field (at $\theta = \pi/2$) at the interface with the core (which exhibits a uniform field $B^3 = \gamma_{\mathrm{III}}B_0$):

$$\begin{cases} \dfrac{2c\gamma_{\mathrm{III}}B_0}{3}(a-b) = \gamma_{\mathrm{III}}B_0 & \rightarrow \quad a - b = \dfrac{3}{2c} \\ \dfrac{2c\gamma_{\mathrm{III}}B_0}{3}\left(a + \dfrac{b}{2}\right) = c\gamma_{\mathrm{III}}B_0 & \rightarrow \quad a + \dfrac{b}{2} = \dfrac{3}{2} \end{cases} \tag{A.26}$$

which gives:

$$\begin{cases} a = 1 + \dfrac{1}{2c} \\ b = 1 - \dfrac{1}{c} \end{cases} \tag{A.27}$$

It should be noted that these coefficients are again very similar to the ones determined in the previous section (b is identical and a is slightly different but is actually the same

when considering large contrast of permeability which is the case here).
The volumetric loss density $Q_{\mathrm{III}}^{\mathrm{bi}}$ can be obtained by using (A.3):

$$Q_{\mathrm{III}}^{\mathrm{bi}} = \frac{3\sigma\pi f^2}{2R_1^3}\int_{R_3}^{R_2}\int_0^{\pi}\int_0^{2\pi} A_\phi(r,\theta)^2 r^2 \sin\theta \mathrm{d}r\mathrm{d}\theta\mathrm{d}\phi \tag{A.28}$$

which expands to:

$$Q_{\mathrm{III}}^{\mathrm{bi}} = \frac{4c^2\gamma_{\mathrm{III}}^2}{9R_1^3}\sigma\pi^2 f^2 B_0^2 \int_{R_3}^{R_2}\left(ar - \frac{bR_3^3}{r^2}\right)^2 r^2\mathrm{d}r \tag{A.29}$$

Using the identities of the radii ratios, the EC loss density is:

$$Q_{\mathrm{III}}^{\mathrm{bi}} = \frac{4}{45}\left(1-\chi_1\right)^{5/3} c^2\gamma^2\lambda_{\mathrm{III}} R_1^2\sigma\pi^2 f^2 B_0^2 \tag{A.30}$$

with λ_{III} a dimensionless parameter equal to:

$$\lambda_{\mathrm{III}} = a^2 - (1-p)^2\left(5b^2 + \frac{5ab}{1-p} + \frac{a^2-5ab-5b^2}{\sqrt[3]{1-p}}\right) \tag{A.31}$$

Appendix A.6. Simplification for large contrasts

The expressions of the losses can be simplified when considering large contrast values, which is the case in this study ($c = 1000$). The expressions for γ_{I}, γ_{II} and γ_{III} can then be approximated to:

$$\begin{cases} c^2\gamma_{\mathrm{I}}^2 \approx \dfrac{1}{(1-\chi_1)^2p^2} \\ c^2\gamma_{\mathrm{II}}^2 \approx \dfrac{16}{(2-\chi_1)^2p^2} \\ c^2\gamma_{\mathrm{III}}^2 \approx \dfrac{81}{4(3-2\chi_1)^2p^2} \end{cases} \tag{A.32}$$

For the same reasons (large contrast c), a and b coefficients can be approximated to unity. Then, λ and λ_{III} can be simplified into:

$$\begin{cases} \dfrac{\lambda}{p^2} \approx 1 - 2\left(\dfrac{1}{p}-1\right)\left(1+\left(\dfrac{1}{p}-1\right)\ln(1-p)\right) = \Phi \\ \dfrac{\lambda_{\mathrm{III}}}{p^2} \approx 1 - 3\left(\dfrac{1}{p}-1\right)\left(1+3\left(\dfrac{1}{p}-1\right)\left(1-\dfrac{1}{\sqrt[3]{1-p}}\right)\right) = \Phi_{\mathrm{III}} \end{cases} \tag{A.33}$$

which finally leads to:

$$\begin{cases} Q_{\mathrm{I}}^{\mathrm{bi}} \approx \dfrac{1}{4}\Phi R_1^2\sigma\pi^2 f^2 B_0^2 \\ Q_{\mathrm{II}}^{\mathrm{bi}} \approx 2\left(\dfrac{1-\chi_1}{2-\chi_1}\right)^2 \Phi R_1^2\sigma\pi^2 f^2 B_0^2 \\ Q_{\mathrm{III}}^{\mathrm{bi}} \approx \dfrac{9}{5}\dfrac{(1-\chi_1)^{5/3}}{(3-2\chi_1)^2}\Phi_{\mathrm{III}} R_1^2\sigma\pi^2 f^2 B_0^2 \end{cases} \tag{A.34}$$

Appendix A.7. Equivalence to the real composite

The losses determined for the doubly coated cylinder/sphere assemblage do not directly correspond to the losses exhibited by a hollow square/cube composite because the size R_1 needs to be set related to ℓ. It has been shown in the literature that the losses in a cylindrical conductive material (with radius R) are:

$$\begin{cases} Q_{\mathrm{I}}^{\mathrm{cyl}} = \dfrac{1}{4} R^2 \sigma \pi^2 f^2 B^2 \\ Q_{\mathrm{II}}^{\mathrm{cyl}} = \dfrac{1}{2} R^2 \sigma \pi^2 f^2 B^2 \end{cases} \tag{A.35}$$

For a sphere (with radius R), it is:

$$Q_{\mathrm{III}}^{\mathrm{sph}} = \frac{1}{5} R^2 \sigma \pi^2 f^2 B^2 \tag{A.36}$$

Similarly, the losses in a square conductive material (with size L) are:

$$\begin{cases} Q_{\mathrm{I}}^{\mathrm{sq}} = \dfrac{9}{128} L^2 \sigma \pi^2 f^2 B^2 \\ Q_{\mathrm{II}}^{\mathrm{sq}} = \dfrac{1}{6} L^2 \sigma \pi^2 f^2 B^2 \end{cases} \tag{A.37}$$

And in a cube (size L), it is:

$$Q_{\mathrm{III}}^{\mathrm{cub}} = \frac{9}{128} L^2 \sigma \pi^2 f^2 B^2 \tag{A.38}$$

In order to make both structures exhibit the same level of losses, the sizes must satisfy:

$$\begin{cases} R^2 = \dfrac{9L^2}{32} & \text{for I} \\ R^2 = \dfrac{L^2}{3} & \text{for II} \\ R^2 = \dfrac{45L^2}{128} & \text{for III} \end{cases} \tag{A.39}$$

For the hollow square/cube structures, the EC loss density is assumed to be similar to the one in a bi-coated cylinder/sphere assemblage with a size chosen according to previous equation.
It finally gives:

$$\begin{cases} Q_{\mathrm{I}}^{\beta} = \dfrac{9}{128} \Phi Q_0 \\ Q_{\mathrm{II}}^{\beta} = \dfrac{2}{3} \left(\dfrac{1-\chi_1}{2-\chi_1} \right)^2 \Phi Q_0 \\ Q_{\mathrm{III}}^{\beta} = \dfrac{81}{128} \dfrac{(1-\chi_1)^{5/3}}{(3-2\chi_1)^2} \Phi_{\mathrm{III}} Q_0 \end{cases} \tag{A.40}$$

with:

$$Q_0 = \pi^2 \sigma f^2 \ell^2 B_0^2 \tag{A.41}$$

Appendix A.8. Consistency with the α configuration

It should be noted that these formulae for the β configuration are consistent with those for the α one. Indeed, the α configuration can be seen as a special β one with no core, which actually means that p is equal to 1 (because $\chi_2 = 1 - \chi_1$). Since Φ and Φ_{III} are equal to 1 in that case, the EC loss density for α configuration can be recovered, leading to the equations given in (12).

References

[1] Daniel Gay. *Composite Materials: Design and Applications*. CRC Press, 3rd edition, July 2014.

[2] Graeme W. Milton. *The Theory of Composites*. Cambridge University Press, 2002.

[3] H. Shokrollahi and K. Janghorban. Soft magnetic composite materials (SMCs). *Journal of Materials Processing Technology*, 189(1):1–12, Jul 2007.

[4] Marco Actis Grande, Luca Ferraris, Fausto Franchini, and Emir Pošković. New SMC materials for small electrical machine with very good mechanical properties. *IEEE Transactions on Industry Applications*, 54(1):195–203, Jan 2018.

[5] E. A. Périgo, B. Weidenfeller, P. Kollár, and J. Füzer. Past, present, and future of soft magnetic composites. *Applied Physics Reviews*, 5(3):031301, Jul 2018.

[6] Bogdan Viorel Neamţu, Alexandru Opriş, Peter Pszola, Florin Popa, Traian Florin Marinca, Nicolae Vlad, and Iionel Chicinaş. Preparation and characterisation of soft magnetic composites based on Fe fibres. *Journal of Materials Science*, 55(4):1414–1424, Feb 2020.

[7] Katie Jo Sunday and Mitra L. Taheri. Soft magnetic composites: recent advancements in the technology. *Metal Powder Report*, 72(6):425–429, Nov 2017.

[8] Olivier de la Barrière, Martino LoBue, and Frédéric Mazaleyrat. Semianalytical and analytical formulas for the classical loss in granular materials with rectangular and elliptical grain shapes. *IEEE Transactions on Magnetics*, 50(10):1–8, Oct 2014.

[9] Xiaotao Ren, Romain Corcolle, and Laurent Daniel. A homogenization technique to calculate eddy current losses in soft magnetic composites using a complex magnetic permeability. *IEEE Transactions on Magnetics*, 52(12):1–9, Dec 2016.

[10] Akito Maruo and Hajime Igarashi. Analysis of magnetic properties of soft magnetic composite using discrete element method. *IEEE Transactions on Magnetics*, 55(6):1–5, Jun 2019.

[11] Innocent Niyonzima, Ruth V. Sabariego, Patrick Dular, and Christophe Geuzaine. Nonlinear computational homogenization method for the evaluation of eddy currents in soft magnetic composites. *IEEE Transactions on Magnetics*, 50(2):61–64, Feb 2014.

[12] Joonas Vesa and Paavo Rasilo. Producing 3-D imitations of soft magnetic composite material geometries. *IEEE Transactions on Magnetics*, 55(10):1–10, Oct 2019.

[13] Romain Corcolle, Xiaotao Ren, and Laurent Daniel. Effective properties and eddy current losses of soft magnetic composites. *Journal of Applied Physics*, 129(1):015103, Jan 2021.

[14] J. Vesa and P. Rasilo. Permeability and resistivity estimations of smc material particles from eddy current simulations. *Journal of Magnetism and Magnetic Materials*, 524:167663, Apr 2021.

[15] Hayaho Sato and Hajime Igarashi. 3-d analysis of soft magnetic composite using discrete element method in frequency domain. *IEEE Transactions on Magnetics*, 57(6):1–4, Jun 2021.

[16] Xiaoyan Shi, Xuyong Chen, Kun Wan, Bowei Zhang, Pengtao Duan, Hua Zhang, Xudong Zeng, Wei Liu, Hailin Su, Zhongqiu Zou, and et al. Enhanced magnetic and mechanical properties of gas atomized fe-si-al soft magnetic composites through adhesive insulation. *Journal of Magnetism and Magnetic Materials*, 534:168040, Sep 2021.

[17] Jinghui Wang, Shengqiang Song, Haibo Sun, Guihua Hang, Zhengliang Xue, Ce Wang, Weihong Chen, and Dongchu Chen. Insulation layer design for soft magnetic composites by synthetically

comparing their magnetic properties and coating process parameters. *Journal of Magnetism and Magnetic Materials*, 519:167496, Feb 2021.

[18] Kaili Li, Danni Cheng, Hongya Yu, and Zhongwu Liu. Process optimization and magnetic properties of soft magnetic composite cores based on phosphated and mixed resin coated Fe powders. *Journal of Magnetism and Magnetic Materials*, 501:166455, May 2020.

[19] Jian Wang, Xin Liu, Jian Mo, Xinhua Mao, Xi'an Fan, and Zigui Luo. The influence of doping Ti on the microstructure and magnetic performances of Fe-6.5Si soft magnetic composites. *Journal of Alloys and Compounds*, 766:769–774, Oct 2018.

[20] Patrick Lemieux, Roderick Guthrie, and Mihaiela Isac. Optimizing soft magnetic composites for power frequency applications and power-trains. *JOM*, 64(3):374–387, Mar 2012.

[21] Mikhail Osanov and James K. Guest. Topology optimization for architected materials design. *Annual Review of Materials Research*, 46(1):211–233, Jul 2016.

[22] V. Chaudhary, S. A. Mantri, R. V. Ramanujan, and R. Banerjee. Additive manufacturing of magnetic materials. *Progress in Materials Science*, 114:100688, Oct 2020.

[23] Dongdong Gu, Xinyu Shi, Reinhart Poprawe, David L. Bourell, Rossitza Setchi, and Jihong Zhu. Material-structure-performance integrated laser-metal additive manufacturing. *Science*, 372(6545), May 2021.

[24] Chao Ding, Shengchang Lu, Lanbing Liu, Khai D. T. Ngo, and Guo-Quan Lu. Additive manufacturing of hetero-magnetic coupled inductors. *IEEE Transactions on Components, Packaging and Manufacturing Technology*, 11(6):1028–1034, Jun 2021.

[25] Christopher Igwe Idumah. Novel trends in magnetic polymeric nanoarchitectures. *Polymer-Plastics Technology and Materials*, 60(8):830–848, May 2021.

[26] S. L. Sing, S. Huang, G. D. Goh, G. L. Goh, C. F. Tey, J. H. K. Tan, and W. Y. Yeong. Emerging metallic systems for additive manufacturing: In-situ alloying and multi-metal processing in laser powder bed fusion. *Progress in Materials Science*, 119:100795, Jun 2021.

[27] J. C. Maxwell-Garnett. Colours in metal glasses and in metallic films. *Philos. Trans. R. Soc. London Sect. A*, 203(359-371):385–420, 1904.

[28] Xiaotao Ren, Romain Corcolle, and Laurent Daniel. Bounds and estimates on eddy current losses in soft magnetic composites. *Journal of Applied Physics*, 123(23):235109, Jun 2018.

[29] Z. Hashin and S. Shtrikman. A variational approach to the theory of the effective magnetic permeability of multiphase materials. *Journal of Applied Physics*, 33(10):3125–3131, 1962.

[30] A.H Sihvola. *Electromagnetic Mixing Formulas and Applications.* Institution of Electrical Engineers, 1999.

[31] Xiaotao Ren, Romain Corcolle, and Laurent Daniel. A 2d finite element study on the role of material properties on eddy current losses in soft magnetic composites. *The European Physical Journal Applied Physics*, 73(22):20902, Feb 2016.

[32] Romain Corcolle and Laurent Daniel. 3-d semi-analytical homogenization model for soft magnetic composites. *IEEE Transactions on Magnetics*, 57(7):1–4, Jul 2021.